Springer

Journal of
Mechanical
Science and
Technology

Journal of Mechanical Science and Technology 22 (2008) 1426~1435

www.springerlink.com/content/1738-494x

Effects of fluid-structure interaction on trailing-edge noise

Youngmin Bae, Jae Young Jang and Young J. Moon*

Department of Mechanical Engineering, Korea University, Seoul, 136-713, Korea

(Manuscript Received July 25, 2007; Revised April 1, 2008; Accepted April 1, 2008)

Abstract

This study numerically investigates the effects of fluid-structure interaction (FSI) on the trailing-edge noise, particularly for the cases of wake instability and Karman vortex shedding. The trailing edge is modeled as a flat plate with an elastic cantilever end and its flow-induced vibration is solved by an eigenmode analysis with the Galerkin method. The flow and sound coupled in the FSI analysis are computed on the moving grid by a direct numerical simulation (DNS) procedure. The computed result of wake instability shows that when the first-eigenmode natural frequency ω_n of the cantilever is close to be resonant with the wake characteristic frequency ω_c, the sound pressure level (SPL) is significantly reduced by 20 dB at ω_n/ω_c=0.95, or increased by 15 dB at ω_n/ω_c=1.05, for all angles. For the Karman vortex shedding, a similar frequency modulation occurs via FSI, if ω_n is close to ω_c. The flow and acoustic details are somewhat different for this case but a considerable noise reduction was also possible for angles from -120° to +120°.

Keywords: Trailing-edge noise reduction; Fluid-structure interaction; Frequency modulation; Wake instability; Karman vortex shedding

1. Introduction

Trailing-edge noise is an important source for airfoil or blade noise. It is generated by wake instability, Karman vortex shedding, or edge scattering of the convecting eddies in the turbulent boundary layer [1], the case of which depends on Reynolds number, edge bluntness, or local momentum thickness of the boundary layer close to the edge, etc. On the trailing-edge noise, comprehensive experimental investigation [2], analytical modeling works [3, 4], and computations [5, 6] have been conducted for years. There also have been some efforts to reduce the trailing-edge noise by modifying the blunt trailing-edge profile [7], implementing porous media [8], or adopting a brush to the trailing edge [9]. For rigid bodies, the trailing-edge noise is closely related to the aerodynamic loads due to boundary layer or unsteady flow behind the trailing edge. But, if the body is sufficiently flexible, then it will move in response to a fluctuating force, and this motion consequently changes the flow structure and the radiated sound. This recoil effect was first described by Lighthill [10] and further investigated by Glegg [11]. In their studies, it was shown that when a body of volume V and density ρ_m is moving through a fluid of density ρ_0, a dipole sound strength is determined by,

$$D_i(t) = -G_i(t) + \rho_0 V \dot{u}_i(t) = -G_i(t)(1 - \rho_0 / \rho_m) , \quad (1)$$

where G_i is the fluctuating force applied to the body, $\dot{u}_i$ is the acceleration of the body, and the last term represented by density ratio indicates resistance force by fluid inertia. In the case of $\rho_m \approx \rho_0$, the recoil effect reacting on the fluctuating force should be considered, because the fluid inertia due to the elastic beam motion has substantial effect on radiated sound. For a heavy beam in a light fluid ($\rho_m \gg \rho_0$), however, the acceleration of the body could be neglected so that dipole strength is only determined by loaded fluctuating force G_i.

*Corresponding author. Tel.: +82 2 3290 3358, Fax.: +82 2 926 9290
E-mail address: yjmoon@korea.ac.kr
DOI 10.1007/s12206-008-0401-1

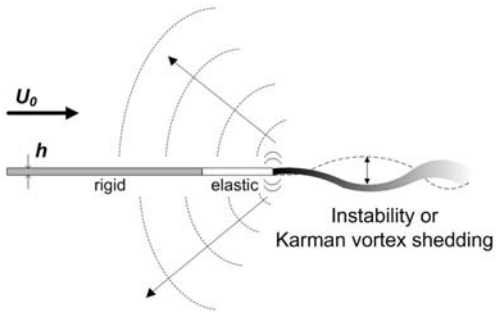

Fig. 1. Schematic of trailing-edge noise with an elastic cantilever end.

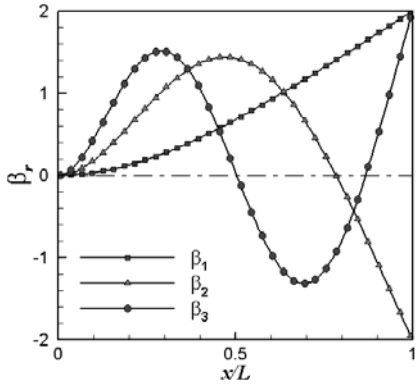

Fig. 2. Modal shapes of the elastic cantilever beam.

In the present study, a fluid-structure interaction (FSI) analysis is conducted to seek for the possibility of reducing the trailing-edge noise, when $\rho_m \gg \rho_0$. As shown in Fig. 1, the trailing edge is modeled as a flat plate with an elastic cantilever end. It is generally known that the natural frequency of the elastic cantilever is as a function of its eigenvalues, speed of sound and fluid density, aspect ratio (h/L, h: thickness, L: length), and elasticity of the cantilever. Our objective is to scrutinize the FSI effects on the trailing-edge noise by varying the elastic properties of the cantilever, especially in the range close to the resonance. The flow-induced vibration of the elastic cantilever is solved by an eigenmode analysis with the Galerkin method, and the flow and sound coupled in the FSI analysis are computed by a direct numerical simulation (DNS) procedure described in section 2. In section 3, the FSI effects on the trailing-edge noise of wake instability and Karman vortex shedding are investigated, with discussion on the frequency modulation and the sound pressure level reductions.

2. Computational methodologies

2.1 Beam equation

The vertical displacement of the elastic cantilever is solved by the beam equation [12],

$$\frac{\partial^2}{\partial x^2}\left[EI(x)\frac{\partial^2 y(x,t)}{\partial x^2}\right] + m(x)\frac{\partial^2 y(x,t)}{\partial t^2} = f(x,t), \quad 0 < x < L \tag{2}$$

where EI (x) is a flexural rigidity, m (x) is the mass per unit length, f (x,t) represents the force distributed over the elastic region, and L is the length of the trailing-edge. The forces on the elastic cantilever beam are usually involved with pressure and shear stress, but it is assumed that shear stress is negligible compared to pressure.

In this study, the flow-induced vibration is solved by an eigenmode analysis with the Galerkin method,

$$y(x,t) = \sum_{r=1}^{\infty} Y_r(x)\eta_r(t), \tag{3}$$

where r is the mode number, Y_r (x) and η_r (t) represent the modal shape and coordinates, respectively. By substituting Eq. (3) into Eq. (2) and applying an orthogonality of the natural modes, an ordinary differential equation of the modal coordinates can be derived:

$$\ddot{\eta}_r(t) + \omega_r^2\eta_r(t) = \int_0^L Y_r(x) f(x,t)dx, \quad r = 1,2,\cdots \tag{4}$$

An analytic solution for the modal shape, Y_r (x) [13] is obtained by employing a fixed left-end boundary condition for the cantilever beam, which is written as

$$Y_r(x) = \cosh\beta_r x - \cos\beta_r x - \sigma_r(\sinh\beta_r x - \sin\beta_r x), \tag{5}$$

where

$$\sigma_r = \frac{\sinh\beta_r L - \sin\beta_r L}{\cosh\beta_r L + \cos\beta_r L}, \tag{6}$$

and the eigenvalues of the cantilever beam with a fixed left-end can be calculated by

$$\cos\beta_r L \cosh\beta_r L + 1 = 0 \,. \tag{7}$$

For approximations, only three eigenvalues are used: $\beta_1 L$=1.87510, $\beta_2 L$ =4.69409, and $\beta_3 L$ =7.85476. The corresponding modal shapes obtained by Eq. (5) are shown in Fig. 2.

2.2 Direct numerical simulation

With the time-dependent displacement of the cantilever beam, the flow and sound around the trailing edge with fluid-structure interactions (FSI) are directly solved by the full two-dimensional compressible Navier-Stokes equations,

$$\frac{\partial Q}{\partial t} + \frac{\partial E}{\partial x} + \frac{\partial F}{\partial y} = \frac{\partial E_v}{\partial x} + \frac{\partial F_v}{\partial y} \,, \tag{8}$$

where

$$Q = \begin{bmatrix} \rho \\ \rho u \\ \rho v \\ \rho e \end{bmatrix}, \quad E = \begin{bmatrix} \rho u \\ \rho u^2 + p \\ \rho uv \\ u(e+p) \end{bmatrix}, \quad F = \begin{bmatrix} \rho v \\ \rho uv \\ \rho v^2 + p \\ v(e+p) \end{bmatrix},$$
$$E_v = \begin{bmatrix} 0 \\ \tau_{xx} \\ \tau_{xy} \\ u\tau_{xx} + v\tau_{xy} \end{bmatrix}, \quad F_v = \begin{bmatrix} 0 \\ \tau_{xy} \\ \tau_{yy} \\ u\tau_{xy} + v\tau_{yy} \end{bmatrix} \tag{9}$$

and τ_{xx}, τ_{yy}, and τ_{xy} indicate viscous stress terms.

In order to include the effects of wall deformation of the elastic trailing edge, the governing equations are solved in a moving coordinate system. The components of the transformation matrix between the physical space (x, y, t) and the computational space (ξ, η, τ) are defined as

$$\begin{bmatrix} d\tau \\ d\xi \\ d\eta \end{bmatrix} = \begin{bmatrix} 1 & 0 & 0 \\ \xi_t & \xi_x & \xi_y \\ \eta_t & \eta_x & \eta_y \end{bmatrix} \begin{bmatrix} dt \\ dx \\ dy \end{bmatrix}, \tag{10}$$

where

$$\xi_x = \frac{y_\eta}{J}, \quad \xi_y = -\frac{x_\eta}{J}, \quad \eta_x = -\frac{y_\xi}{J}, \quad \eta_y = \frac{x_\xi}{J}$$
$$\xi_t = \frac{(-x_\tau y_\eta + x_\eta y_\tau)}{J}, \quad \eta_t = \frac{(x_\tau y_\xi - x_\xi y_\tau)}{J}, \quad \tau = t \tag{11}$$

Here, $J=x_\xi y_\eta - x_\eta y_\xi$, and x_τ and y_τ represent the moving grid velocities at each control surface.

The governing equations are spatially discretized with a sixth-order compact finite difference scheme [14] and integrated in time by a four-stage Runge-Kutta method. The first and second derivatives with respect to x are implicitly calculated with a five stencil, i.e.,

$$\alpha_1 f'_{i-1} + f'_i + \alpha_1 f'_{i+1} = a_1 \frac{f_{i+1} - f_{i-1}}{2\Delta x} + b_1 \frac{f_{i+2} - f_{i-2}}{4\Delta x}$$
$$\alpha_2 f''_{i-1} + f''_i + \alpha_2 f''_{i+1} = a_2 \frac{f_{i+1} - 2f_i + f_{i-1}}{\Delta x^2} + b_2 \frac{f_{i+2} - 2f_i + f_{i-2}}{4\Delta x^2} \tag{12}$$

where α_1=1/3, α_2=2/11, a_1=14/9, b_1=1/9, a_2=12/11, and b_2=3/11.

Practically, when using a high order scheme to the stretched meshes, numerical instability is encountered due to numerical truncations or failure of capturing high wave-number phenomena. Thus, a tenth-order spatial filtering proposed by Gaitonde et al. [15] is applied every iteration to suppress the high frequency errors that might be caused by grid non-uniformity. For the far-field boundary condition, an energy transfer and annihilation (ETA) boundary condition [16] with buffer zone is used for eliminating any reflection of the out-going waves.

2.3 Moving grid system

To resolve the interaction process among flow, acoustics, and structure, the full compressible Navier-Stokes equations, Eq. (8) are directly solved on the moving grid with the high-order numerical schemes described in section 2.2. In many practical applications involving deforming meshes, the grid speeds, x_τ and y_τ in Eq. (11) are not known analytically and must be approximated to the desired degree of accuracy with the evolving grid coordinates at several time levels.

For this case, the computed grid speeds are approximated as

$$x_\tau = [(1+\phi)x^{n+1} - (1+2\phi)x^n + \phi x^{n-1}]/\Delta t \,, \tag{13}$$

where ϕ indicates the time differencing schemes listed in Table 1. The time differencing schemes have different accuracy with the time-integration method used for Eq. (8). For the four-stage Runge-Kutta method (RK4), the governing equations are integrated in time from n to n+1. In this case, the moving grid speeds should be approximated at n+1/2, for which

Table 1. Temporal accuracy of the time differencing schemes for moving grids.

ϕ	Approximation x_τ	Accuracy (RK4)	Accuracy (Leapfrog)
-1	$\frac{(x^n - x^{n-1})}{\Delta t}$	O(Δt)	O(Δt/2)
0	$\frac{(x^{n+1} - x^n)}{\Delta t}$	O(Δt^2)	O(-Δt/2)
-1/2	$\frac{(x^{n+1} - x^{n-1})}{2\Delta t}$	O(Δt/2)	O(Δt^2)
1/2	$\frac{(3x^{n+1} - 4x^n + x^{n-1})}{2\Delta t}$	O(-Δt/2)	O(Δt)

the Taylor's series are expanded as

$$
\begin{aligned}
f^{n+1} &= f(t) + \frac{\Delta t}{2} f'(t) + \frac{1}{2!}\left(\frac{\Delta t}{2}\right)^2 \\
&\quad f''(t) + \frac{1}{3!}\left(\frac{\Delta t}{2}\right)^3 f'''(t) + O\left(\Delta t^4\right) \\
f^{n} &= f(t) - \frac{\Delta t}{2} f'(t) + \frac{1}{2!}\left(\frac{\Delta t}{2}\right)^2 \\
&\quad f''(t) - \frac{1}{3!}\left(\frac{\Delta t}{2}\right)^3 f'''(t) + O\left(\Delta t^4\right) \\
f^{n-1} &= f(t) - \frac{3\Delta t}{2} f'(t) + \frac{1}{2!}\left(\frac{3\Delta t}{2}\right)^2 \\
&\quad f''(t) - \frac{1}{3!}\left(\frac{3\Delta t}{2}\right)^3 f'''(t) + O\left(\Delta t^4\right).
\end{aligned}
\tag{14}
$$

Consequently, $\phi = 0$ only yields the second-order temporal accuracy as shown in Table 1.

For the Leapfrog method, the governing equations are integrated in time from n-1 to n+1. So, the moving grid speeds should be approximated at n, for which the Taylor's series are expanded as

$$
\begin{aligned}
f^{n+1} &= f(t) + \Delta t f'(t) + \frac{1}{2!}(\Delta t)^2 \\
&\quad f''(t) + \frac{1}{3!}(\Delta t)^3 f'''(t) + O\left(\Delta t^4\right) \\
f^{n-1} &= f(t) - \Delta t f'(t) + \frac{1}{2!}(\Delta t)^2 \\
&\quad f''(t) - \frac{1}{3!}(\Delta t)^3 f'''(t) + O\left(\Delta t^4\right).
\end{aligned}
\tag{15}
$$

For this case, the second-order temporal accuracy is only achieved for $\phi = -1/2$. It is also worth noting that the three-level time differencing ($\phi = 1/2$) is only first-order accurate for both RK4 and Leapfrog methods.

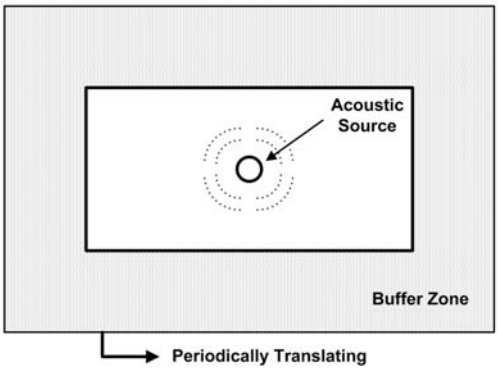

Fig. 3. Computation of acoustic wave propagation on the oscillating grid.

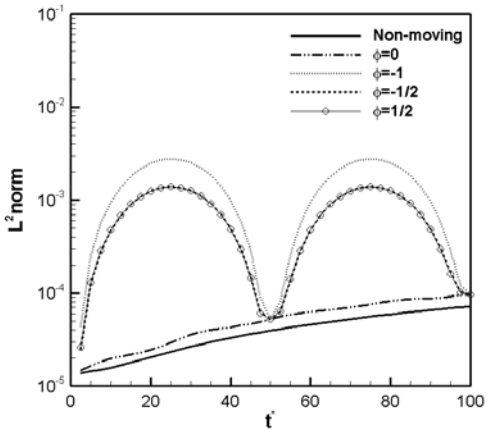

Fig. 4. Time history of L^2-error for RK4 method.

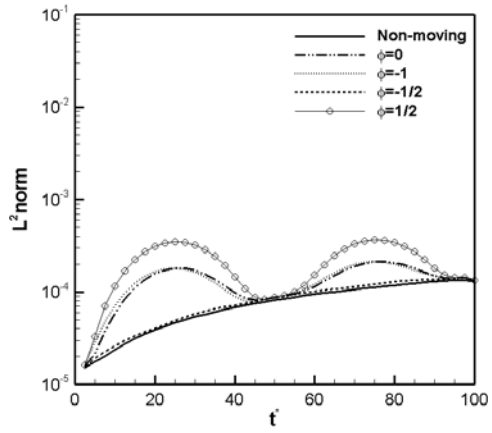

Fig. 5. Time history of L^2-error for Leapfrog method.

Here, two-dimensional acoustic wave propagation is computed on the moving grid to test the accuracy of the time differencing schemes listed in Table 1. As

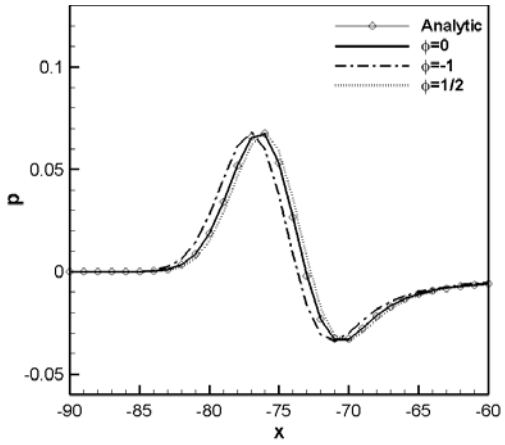

Fig. 6. Pressure distribution along the y=0 line at t=75.

sketched in Fig. 3, the linearized Euler equations (LEE) are solved on the non-deforming but oscillating cartesian grid (Δx=Δy=1), with a grid speed defined as

$$u(t) = 2\pi f_0 A \cos(2\pi f_0 t)\,, \tag{16}$$

where A (magnitude) is 10 and f_0 (oscillation frequency) is 0.02. The LEE calculation was continued until t=100, using the time steps, Δt=1/4 and Δt=1/32 for RK4 and Leapfrog methods, respectively.

As shown in Figs. 4 and 5, the second-order accurate time differencing schemes yield L^2 errors close to the non-moving case, while substantial errors are introduced by the first-order schemes. This is due to the inaccurately evaluated characteristic speeds, $u-\tilde{x}_\tau$, $(u+c)-\tilde{x}_\tau$, and $(u-c)-\tilde{x}_\tau$, where $\tilde{x}_\tau$ is the grid speed approximated by the time differencing scheme listed in Table 1. Fig. 6 compares the pressure distributions at t=75 calculated by different ϕ's with RK4 method. A noticeable phase difference is observed with the moving grid because of the time differencing errors.

3. Results and discussion

3.1 Wake instability

By the Kelvin-Helmholtz instability, a wake behind the plate becomes unstable at Reynolds number based on the plate thickness h, Re_h=200 and free-stream Mach number, M=0.4. As a result, the unstable wake produces a distinct dipole tone at the trailing edge. As depicted in Fig. 7, a computational domain is set from

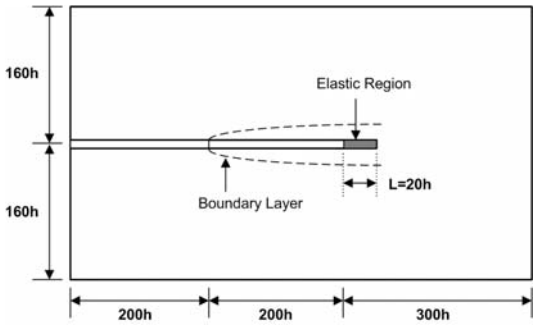

Fig. 7. Computational domain for the trailing-edge noise with an elastic cantilever end.

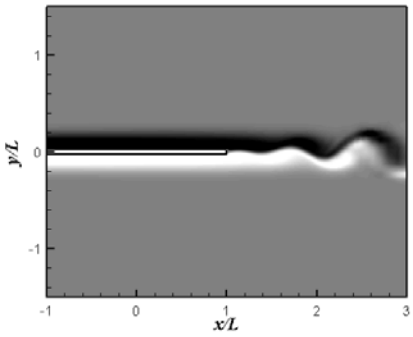

(a)

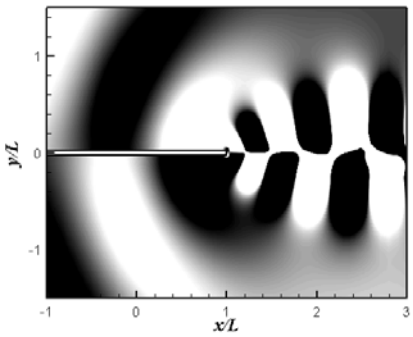

(b)

Fig. 8. Trailing-edge noise by wake instability (rigid case): a) vorticity (40 contours between -5 and 5), b) pressure fluctuation (40 contours between -0.0005 and 0.0005).

-400h to 300h in the streamwise direction and ±160h in the normal direction, and 301×211 mesh points are non-uniformly distributed for DNS of flow and acoustics. A no-slip boundary condition is applied along the solid wall, except the region from -400h to -200h, where a slip condition is used. In order to induce the wake instability, a laminar boundary layer over the plate is disturbed at t=0 by a vortical distur-

bance defined as

$$u'(x,y)=\frac{1}{2h}U_0(y-y_0)\exp\left(0.5\left(1-\left(\sqrt{(x-x_0)^2+(y-y_0)^2}/h\right)^2\right)\right)$$
$$v'(x,y)=-\frac{1}{2h}U_0(x-x_0)\exp\left(0.5\left(1-\left(\sqrt{(x-x_0)^2+(y-y_0)^2}/h\right)^2\right)\right), \quad (17)$$

where $(x_0,y_0)= (0,0.1L)$ and L is the cantilever length.

First, a 'rigid' body case is computed for finding a reference solution. Fig. 8 shows the instantaneous vorticity contours of unstable wake and its resulting acoustic field. The pressure fluctuation monitored at $(x/L,y/L)= (0,2)$ indicates that the characteristic frequency, $St_h=fh/U_0$ is approximately 0.046 (or $\omega_c=2\pi fL/c_\infty \approx 2.31$) and the sound pressure level (SPL) of the peak is predicted as 109 dB (see Fig. 9). This frequency is found very close to the most unstable wake instability mode [1].

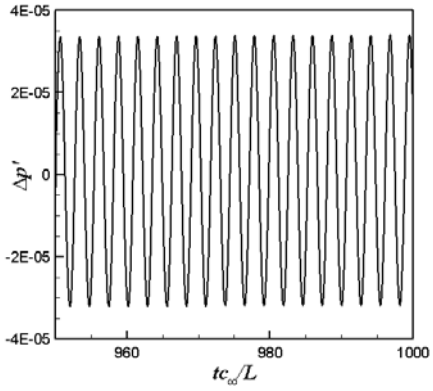

(a)

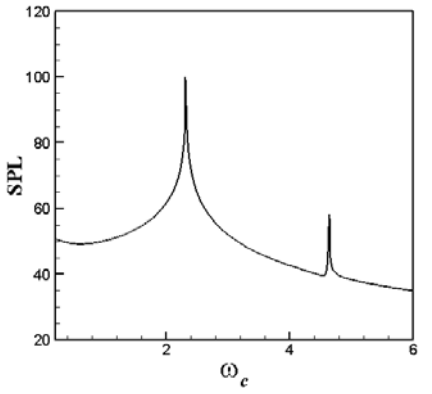

(b)

Fig. 9. Time variation of pressure fluctuations and SPL spectrum (rigid case) at $(x/L,y/L)=(0,2)$.

To examine the FSI effects on the trailing-edge noise, the rigid part of the trailing edge is now replaced by an elastic cantilever with L/h=20, and a parametric study is conducted by varying the elasticity (E) of the cantilever. A non-dimensionalized, natural frequency of the elastic cantilever is written as

$$\omega_r=(\beta_r L)^2\frac{h}{c_\infty L}\sqrt{\frac{E}{12\rho}}, \quad (18)$$

where β_r, c_∞, ρ, h/L, and E denote eigenvalues, speed of sound, fluid density, aspect ratio, and elasticity of the cantilever, respectively. In this study, the FSI effects on the trailing-edge noise are scrutinized for the test cases summarized in Table 2.

The tip displacement response of the elastic cantilever under FSI condition is plotted in Fig. 10 against ω_{1n}/ω_c. Here, ω_{1n} is the first eigenmode natural frequency of the elastic cantilever and ω_c is the characteristic frequency of the wake. Although the tip displacement itself is quite small (e.g. $7\times10^{-4}h$), it is noticeably amplified at each eigen-resonant frequency (i.e. $\omega_{1n}/\omega_c=1$, $\omega_{2n}/\omega_c=1$, and $\omega_{3n}/\omega_c=1$). It is interesting to note that the maximum tip displacement does not occur at $\omega_n/\omega_c=1$ but at 1.05. This shift may be caused by the non-linear coupling effects between the

Table 2. Test cases for the elastic cantilever beams.

	Density [kg/m^3]	Elasticity [Pa]	ω_1	ω_2	ω_3	ω_1/ω_c
Case A	240	1.91×10^8	0.132	0.825	2.310	0.057
Case B	240	6.39×10^8	0.241	1.510	4.226	0.104
Case C	240	1.50×10^8	0.369	2.310	6.468	0.160
Case D	240	6.72×10^8	0.781	4.896	13.709	0.338
Case E	240	5.87×10^8	2.310	14.477	40.535	1.000
Case F	240	1.36×10^8	3.516	22.034	61.697	1.522

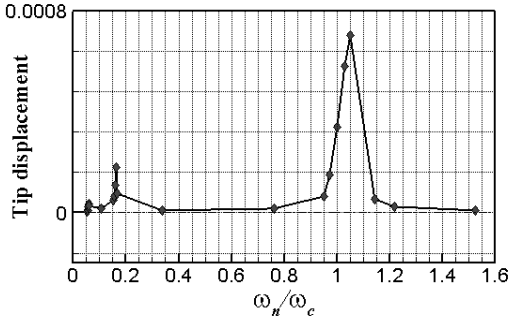

Fig. 10. Tip displacement versus natural frequencies of the elastic cantilever.

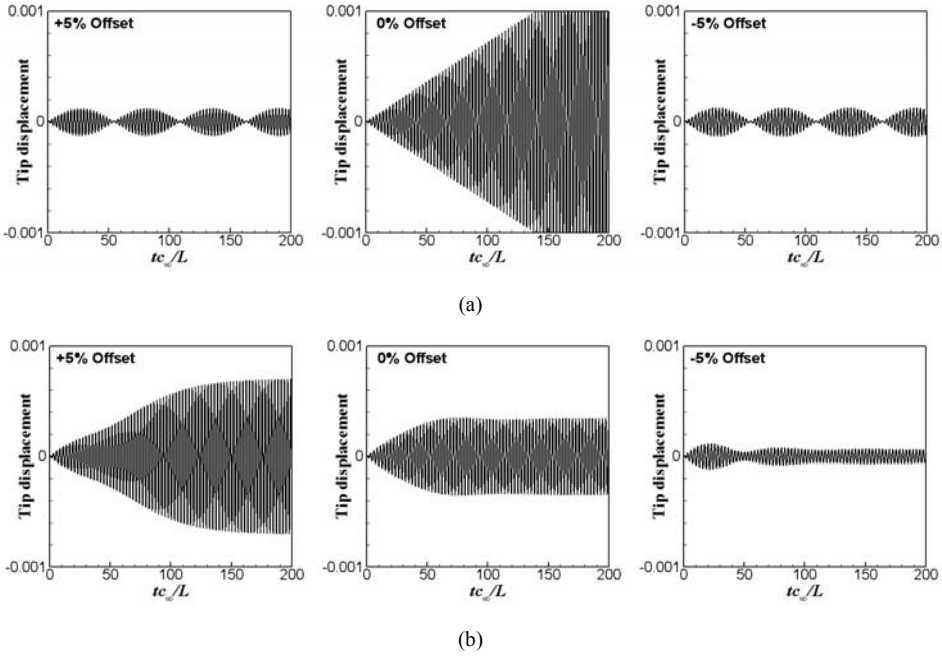

(a)

(b)

Fig. 11. Tip displacement of the elastic cantilever: a) forced vibration and b) fluid-structure interaction (FSI).

unstable wake and the elastic cantilever. To further examine with the non-FSI case, a forced-vibration of the elastic cantilever is computed for an external force defined as

$$f(t) = q(x)\cos(\omega_c t)\,, \tag{19}$$

where ω_c=2.31 and a distributed force $q(x)$ on the cantilever beam is modeled as

$$q(x) = \begin{cases} 0 & , \quad 0 \le x \le 0.5 \\ 0.0024\left(x - 0.5\right)^2 , & 0.5 \le x \le 1 \end{cases} \tag{20}$$

As shown in Fig. 11(a), the tip displacement in forced-vibration continuously diverges at the first eigen-resonant frequency (0% offset), while beats are clearly observed for the ±5% offset cases. Meanwhile, the FSI cases show different dynamical behaviors, as presented in Fig. 11(b). At the resonance frequency, the tip displacement grows initially but converges to an asymptotic value ($3.8\times10^{-4}h$) because fluids act as a damper to the cantilever beam motions. When the frequency is ±5% offset from the wake characteristic frequency, the beats gradually disappear and the tip displacement is either least amplified to $8\times10^{-5}h$ at -5% offset or most amplified to $7\times10^{-4}h$ at

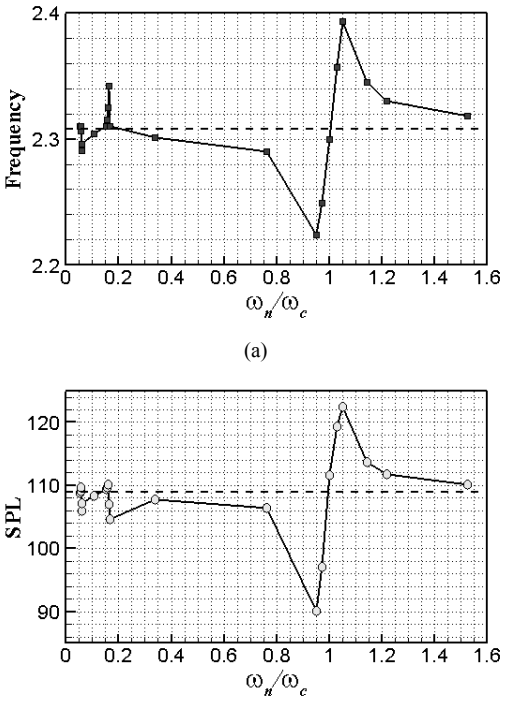

(a)

(b)

Fig. 12. Modulated frequency ω_f and sound pressure level (dB) versus natural frequency of the elastic cantilever (dashed line: rigid case): wake instability.

+5% offset.

It is also found that this dynamical behavior alters the frequency and acoustic characteristics of the elastic cantilever. As shown in Fig. 12(a), the wake frequency is considerably modulated, especially at the first eigen-resonance frequency via FSI effects. When ω_n/ω_c is 0.95, the wake characteristic frequency is altered from 2.31 to 2.22, whereas for ω_n/ω_c=1.05, it changes to 2.39. There are also two small variations at the second and third eigenmodes of the wake characteristic frequency, i.e., ω_n/ω_c=0.160 and ω_n/ω_c=0.057, but their effects are obviously much weaker than the first eigenmode.

As shown in Fig. 12(b), the sound pressure level is also significantly altered by this frequency modulation. When compared to the rigid body case, the trail ing-edge noise monitored at (x/L,y/L)= (0,2) is reduced by 20 dB with the elastic cantilever at ω_n/ω_c=0.95, or increased by 15 dB at ω_n/ω_c=1.05. For completeness, the SPL characteristics are examined for all angles by plotting the directivity patterns of the pressure fluctuations at r=L. As shown in Fig. 13, significant noise reductions occur at ω_n/ω_c= 0.95 for all angles.

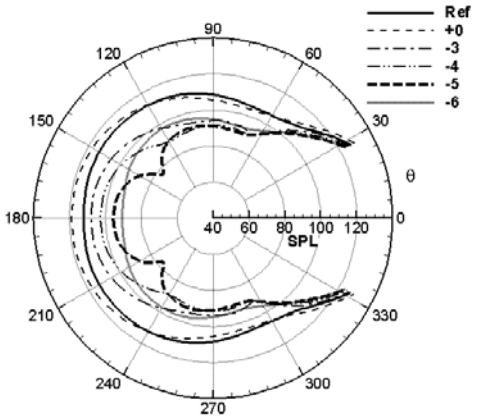

(a)

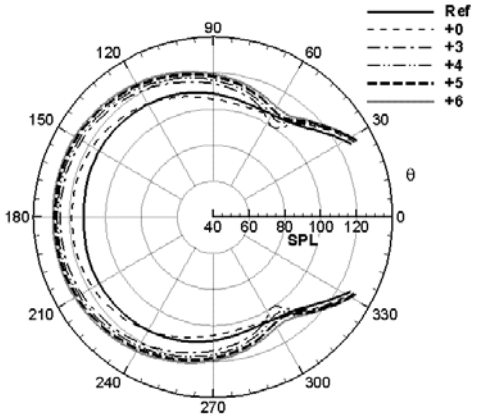

(b)

Fig. 13. SPL directivity patterns for various elastic properties of the cantilever at r=L: wake instability.

3.2 Karman vortex shedding

With a potential reduction of trailing-edge noise via FSI effects, a similar investigation is pursued for the Karman vortex shedding noise. A laminar boundary layer over the plate is considered at Re_h=1000 and M=0.4. The computational domain and grid system are the same as in the last section. A no-slip wall boundary condition is, however, applied from -1.5L so that the boundary layer thickness at the trailing edge is close to 1.2h. This value is an upper limit (laminar) for invocation of the Karman vortex shedding with blunt thickness [1]. In this case, the dipole tone is stronger than the previous case. The computed result for the 'rigid' trailing edge indicates that the characteristic frequency of the vortex shedding occurs at St_h=fh/U_0≈ 0.145 (or ω_c=7.28) and the SPL peak is close to 135dB.

Based on results of wake instability, one can also expect similar frequency modulations and noise reductions via FSI with the elastic cantilever. So, the elastic properties of the cantilever are only selected to have the first eigenmode natural frequency close to the characteristic frequency of the Karman vortex shedding, i.e., ω_c=7.28. As shown in Fig. 14, the frequency modulation also occurs near ω_n/ω_c=1, similar to the wake instability. In this case, a difference between the elastic and rigid trailing edges occurs, when the first-eigenmode natural frequency of the cantilever is ±2% offset from ω_c.

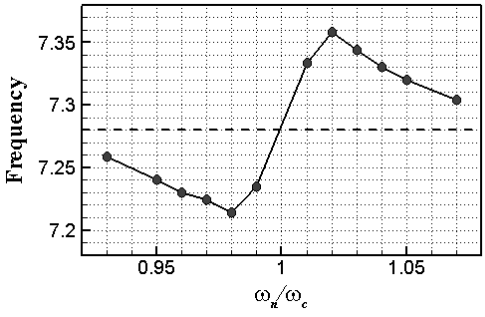

Fig. 14. Modulated frequency ω_f versus natural frequency of the elastic cantilever (dashed line: rigid case): Karman vortex shedding.

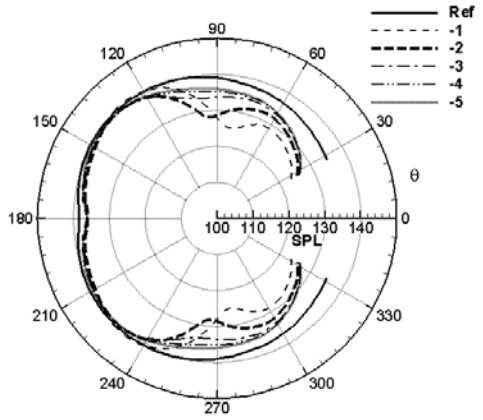

(a)

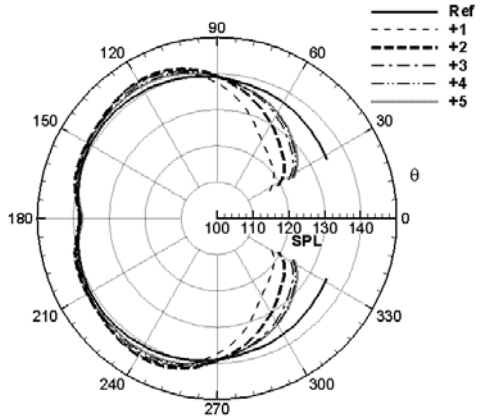

(b)

Fig. 15. SPL directivity patterns for various elastic properties of the cantilever at $r=L$: Karman vortex shedding.

The noise characteristics of the elastic cantilever for the Karman vortex shedding are, however, somewhat different from those for the wake instability. As shown in Fig. 15, the SPL directivity patterns indicate that a significant noise reduction also occurs for angles from -120º to +120º, even for the positive offsets from ω_c. The FSI effects on the trailing-edge noise are not as drastic as in the wake instability because the Karman vortex shedding is a more localized phenomenon near the trailing edge. If the density of the material is changed, then a more pronounced SPL reduction could be expected.

4. Conclusions

The effects of fluid-structure interaction (FSI) on the trailing-edge noise are scrutinized by varying the elastic properties of the cantilever end. For the wake instability, the computed results of DNS with an eigenmode analysis of the beam equation show that when the first-eigenmode natural frequency ω_n of the cantilever is close to be resonant with the wake characteristic frequency ω_c, the sound pressure level (SPL) is significantly reduced at all angles by 20 dB at ω_n/ω_c=0.95, or increased by 15 dB at ω_n/ω_c=1.05. For the Karman vortex shedding, a similar frequency modulation also occurs via FSI, if ω_n is close to ω_c. The flow and acoustic details are somewhat different but a significant noise reduction was also possible for angles from -120º to +120º. The present FSI effects on the trailing-edge noise result from the fact that the first eigenmode of the natural frequency has significant effects on the displacement, frequency modulation and acoustic characteristics of the elastic cantilever.

References

[1] W. K. Blake, Mechanics of Flow-Induced Sound and Vibration, Vol. 1, General concepts and elementary sources, Academic Press, (1986).

[2] T. F. Brooks and T. H. Hodgson, The Trailing-Edge Noise Prediction From Measured Surface Pressure, *Journal of Sound and Vibration,* 78 (1981) 69-117.

[3] M. S. Howe, A Review of the Theory of Trailing-Edge Noise, *Journal of Sound and Vibration,* 61 (1978) 437-465.

[4] M. Roger and S. Moreau, Broadband Self-Noise from Loaded Fan Blades, *AIAA Journal,* 42 (2004) 536-544.

[5] K. W. Chang, J. H. Seo, Y. J. Moon and M. Roger, Prediction of Flat Plat Self-Noise, Proc. of 12th AIAA/CEAS Aeroacoustics Conference (2006) AIAA-Paper 2006-2513.

[6] M. Wang and P. Moin, Wall Modeling in LES of Trailing Edge Flow, Proc. of 2nd International Symposium on Turbulence and Shear Flow Phenomena (2001) 165-170.

[7] A. L. Marsden, M. Wang and B. Mohammadi, Shape Optimization for Aerodynamic Noise Control, Center for Turbulence Research, Annual Research Briefs (2001).

[8] M. R. Khorrami and M. M. Choudhari, Application of Passive Porous Treatment to Slat Trailing Edge Noise, Langley Research Center (2003), NASA/TM 2003-212416.

[9] M. Herr and W. Dobrzynski, Experimental Investigation in Low Noise Trailing Edge Design, Proc. of

10th AIAA/CEAS Aeroacoustics Conference (2004) AIAA-Paper 2004-2804.

[10] M. J. Lighthill, Waves in Fluids, Cambridge University Press, (1978).

[11] S. A. L. Glegg, Sound Radiation from Flexible Blades, *Journal of Sound and Vibration,* 98 (1985) 171-182.

[12] L. Meirovitch, Fundamentals of Vibrations, McGraw-Hill, (2001).

[13] M. P. Paidoussis, Fluid-Structure Interactions, Volume I, Academic Press, (1998).

[14] S. K. Lele, Compact Finite Difference Schemes with Spectral-Like Resolution, *Journal of Computational Physics,* 103 (1992) 16-42.

[15] D. V. Gaitonde, J. S. Shang and J. L. Young, Practical aspects of higher-order numerical schemes for wave propagation phenomena, *International Journal for Numerical Methods in Engineering,* 45 (1999) 1849-1869.

[16] N. B. Edgar and M. R. Visbal, A General Buffer Zone-Type Non-Reflecting Boundary Condition for Computational Aeroacoustics, Proc. of 9th AIAA/CEAS Aeroacoustics Conference (2003) AIAA-Paper 2003-3300.